Electronic Supplementary Information for

Absolute photodissociation cross sections of thermalized methyl vinyl ketone oxide and methacrolein oxide

Yen-Hsiu Lin,[a,b] Kaito Takahashi[a] and Jim Jr-Min Lin*[a,b]*

[a]Institute of Atomic and Molecular Sciences, Academia Sinica, Taipei 10617, Taiwan

[b]Department of Chemistry, National Taiwan University, Taipei 10617, Taiwan.

*Corresponding Authors:

kt@gate.sinica.edu.tw

jimlin@gate.sinica.edu.tw

ORCID:

Kaito Takahashi: 0000-0003-2339-4295

Jim Jr-Min Lin: 0000-0002-8308-2552

1. SUMMARY OF EXPERIMENTAL RESULTS AND CONDITIONS

1.1 Reference Spectra of MVKO, MACRO, IO, and I_2 that Are Used in the Analysis
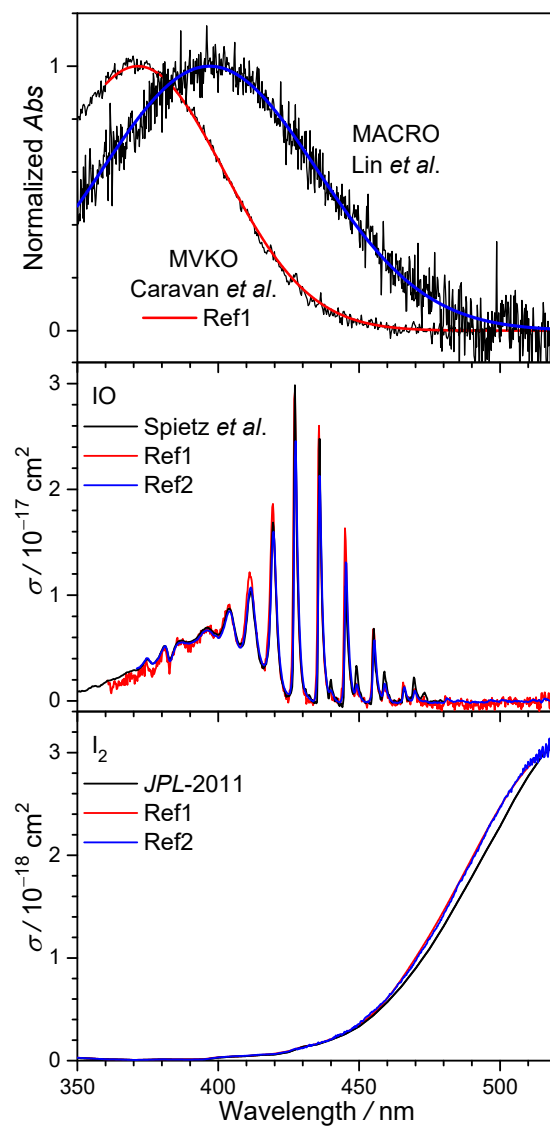

Fig. S1 Reference spectra of MVKO (upper panel), IO (middle panel), and I_2 (lower panel) obtained in this work to properly include the instrument function (mainly the resolution of the spectrometer). Ref1 spectra (red lines) are for the analysis of the MVKO experiments; Ref2 spectra (blue lines) are for the analysis of the MACRO experiments. The MACRO spectrum used in our analysis (upper panel) is the same as the reported Gaussian fit.[1] For comparison, the literature spectra[1-4] are also shown (black lines).

1.2 Summary of the Kinetic Parameters of Relevant Processes

Table S1. Available rate coefficients k, absorption cross sections σ, and/or effective time scales of relevant reactions under the present experimental conditions (at 298 K).

R1	$ICH_2CHCICH_3 + h\nu$ (248 nm) $\rightarrow CH_3(C_2H_3)CI + I$	laser pulse < 20 ns $\sigma = 1.95\times10^{-17}$ cm^2 at 248 nm	Kuo et al.[5]
R2a	$CH_3(C_2H_3)CI + O_2 \rightarrow CH_3(C_2H_3)COO$ (MVKO) + I	$k = (1.7\pm0.07)\times10^{-13}$ cm^3 s^{-1} $[O_2] = 3.2\times10^{17}$ cm^{-3}	Caravan et al.[2]
R2b	$CH_3(C_2H_3)CI + O_2 + M \rightarrow CH_3(C_2H_3)CIOO$ (adduct) + M	$k_{eff} = 5.4\times10^4$ s^{-1}	
R3	$CH_3(C_2H_3)CIOO$ (adduct) $\rightarrow CH_3(C_2H_3)COO$ (MVKO) + I	$k \sim 10^3$ s^{-1}	Lin et al.[6]
R4	MVKO + $h\nu$ (352 nm) $\rightarrow$ MVK + O(^{1}D)	laser pulse < 20 ns, $\sigma = (3.02\pm0.60)\times10^{-17}$ cm^2 at 352 nm	this work
R5	MVKO + X $\rightarrow$ products	depending on the reaction condition	
R6	MVKO $\rightarrow$ products (Unimolecular decomposition)	$k = (70\pm15)$ s^{-1}	Lin et al.[7]
R7	$ICH_2CHCICH_3 + h\nu$ (352 nm) $\rightarrow CH_3(C_2H_3)CI + I$	laser pulse < 20 ns	
R8	O(^{1}D) + M $\rightarrow$ O(^{3}P) + M	$k = 3.1\times10^{-11}$ cm^3 s^{-1} $[M] \sim 3.2\times10^{18}$ cm^{-3} $k_{eff} \sim 10^8$ s^{-1}	JPL 2011[4]
R9	O(^{3}P) + $ICH_2CHCICH_3 \rightarrow CH_3(C_2H_3)CI + IO$	$k > 5\times10^{-11}$ cm^3 s^{-1} $[ICH_2CHCICH_3] = 8\times10^{13}$ cm^{-3} $k_{eff} > 4\times10^3$ s^{-1}	see main text
R10	O(^{3}P) + $C_2H_5I \rightarrow C_2H_5 + IO$ (and other products)	$k = (3.51\pm0.17)\times10^{-11}$ cm^3 s^{-1}	Teruel et al.[8]
R11	O(^{3}P) + 1-$C_3H_7I \rightarrow$ 1-C_3H_7 + IO (and other products)	$k = (3.79\pm0.25)\times10^{-11}$ cm^3 s^{-1}	Teruel et al.[8]
R12	O(^{3}P) + 2-$C_3H_7I \rightarrow$ 2-C_3H_7 + IO (and other products)	$k = (4.97\pm0.28)\times10^{-11}$ cm^3 s^{-1}	Teruel et al.[8]
R13	$NO_2 + h\nu$ (352 nm) $\rightarrow$ NO + O(^{3}P)	$\sigma = 4.53\times10^{-19}$ cm^2 at 352 nm	Bogumil et al.[9]
R14	$ICH_2C(CH_3)CHI + h\nu$ (248 nm) $\rightarrow CH_2=C(CH_3)CHI + I$	laser pulse < 20 ns $\sigma = 2.43\times10^{-17}$ cm^2 at 248 nm	Lin et al.[1]
R15a	$CH_2=C(CH_3)CHI + O_2 \rightarrow CH_2=C(CH_3)CHOO$ (MACRO) + I	$k_{eff} > 4000$ s^{-1} $[O_2] = 3.2\times10^{17}$ cm^{-3}	this work (Fig. 9)[a]
R15b	$CH_2=C(CH_3)CHI + O_2 + M \rightarrow CH_2=C(CH_3)CHIOO$ (adduct) + M	$k > 1.3\times10^{-14}$ cm^3 s^{-1}	
R16	MACRO + $h\nu$ (352 nm) $\rightarrow$ MACR + O(^{1}D)	$\sigma = (1.53\pm0.29)\times10^{-17}$ cm^2 at 352 nm	this work
R17	MACRO + X $\rightarrow$ products	depending on the reaction condition	
R18	MACRO $\rightarrow$ products (Unimolecular decomposition)	$k = 7$ s^{-1}	Lin et al.[1]
R19	O(^{3}P) + $ICH_2C(CH_3)CHI \rightarrow$ IO + products	$k > 5\times10^{-11}$ cm^3 s^{-1} $[ICH_2C(CH_3)CHI] = 4\times10^{13}$ cm^{-3} $k_{eff} > 2\times10^3$ s^{-1}	see main text
R20	$ICH_2C(CH_3)CHI + h\nu$ (352 nm) $\rightarrow CH_2=C(CH_3)CHI + I$	laser pulse < 20 ns	

[a] In Fig. 9, the effective generation rate of MACRO is faster than the frame rate, which is 4000 s^{-1}.
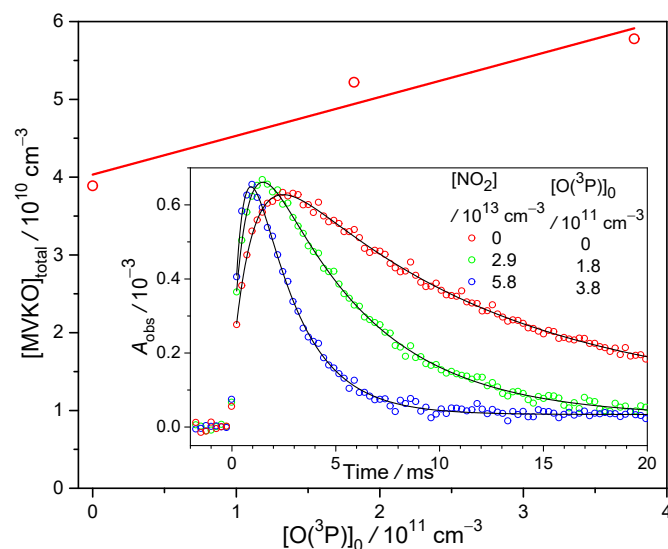
1.3 MVKO from (R9): O(^{3}P) Reaction with the Precursor

Fig. S2 [MVKO]$_{total}$ plotted as a function of estimated [O(^{3}P)]$_0$ (from $NO_2 + h\nu \rightarrow O(^3P) + NO$)[4] in the 1,3-diiodo-but-2-ene/O$_2$/NO$_2$ system photolyzed at 352 nm (without 248-nm laser) at nearly constant [precursor] (8.4×10^{13} cm^{-3}) and $F_{\text{eff\_352}}$ (8.0 mJ cm^{-2}) at 299 K and 99.6 Torr (the data has been corrected for the variations of [precursor] (~9 %) and $F_{\text{eff\_352}}$ (~2%)). [MVKO]$_{total}$ was deduced with the MVKO cross sections determined in this work (see Fig. 7 and related text). Inset: The corresponding time profiles of the peak absorbance signal of MVKO obtained by fitting the spectra at each camera frame. The time zero is set as the 352 nm laser pulse. The black lines show the fitting results of eqn (7)–(8) in the main text.

As shown in Fig. S2, the decay of MVKO becomes faster at higher [NO$_2$], suggesting that MVKO reacts with NO$_2$. We analyzed the data with eqn (7)–(8) to properly account for the effect of the MVKO reactions. Fig. S2 also shows that when other conditions are fixed, higher [MVKO]$_{total}$ is found at higher [NO$_2$] (thus higher [O(^{3}P)]$_0$), indicating the role of (R9). However, the relatively large intercept of Fig. S2 indicates that this channel is minor and the main source of the post-photolysis MVKO is still the channel via (R7).

In addition, more IO radicals have been observed in the reaction system after the 352 nm photolysis when NO$_2$ is present (Fig. S3), further supporting the role of (R9). The observed yield of IO relative to [O(^{3}P)]$_0$ is about 0.25 ± 0.03 (See Table S2).
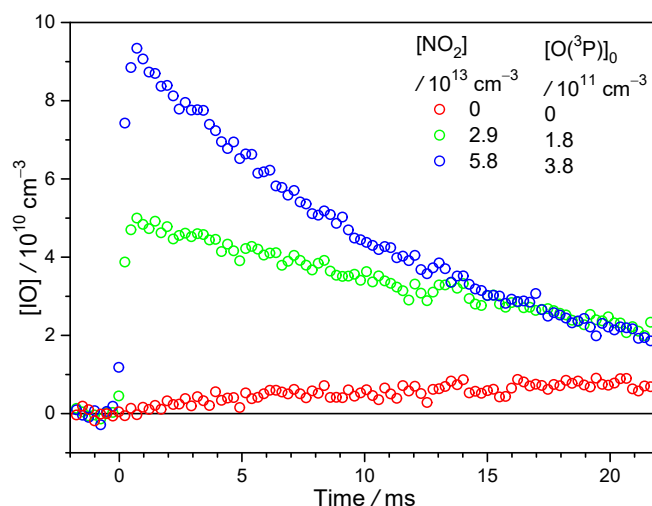
Fig. S3 Time profile of [IO] obtained by fitting the spectra at each camera frame in the 1,3-diiodo-but-2-ene/O_2/NO_2 352-nm photolysis system under various [NO_2] at 299 K and 99.6 Torr. F_{eff_352} = 8.0 mJ cm^{-2}; [precursor] = 8.4×10^{13} cm^{-3}. The time zero is set as the 352 nm photolysis laser. [IO] is derived by comparing with its literature cross sections.[3] [O(^{3}P)]$_0$ is estimated with F_{eff_352}, [NO_2], σ = 4.53×10^{-19} cm^2, ϕ = 1 at 352 nm.[4,9] At [O(^{3}P)]$_0$ = 0, some IO is still produced, likely through the reaction of MVKO + I → MVK + IO. The data are from Exp R2-R4 (Table S2).

Table S2. Summary of the 352 nm photolysis of $ICH_2CHCICH_3$/O_2/NO_2 system and the reaction of $ICH_2CHCICH_3$ with O(^{3}P) for the formation of MVKO. P_{total} = 100 Torr balanced by N_2. P_{O2} = 10 Torr. T = 299 K. F_{eff_352} = 8.0 mJ cm^{-2}.

Exp #	[$ICH_2CHCICH_3$] / 10^{13} cm^{-3}	[NO_2]$_0$ / 10^{13} cm^{-3}	[O(^{3}P)]$_0$ / 10^{11} cm^{-3}	[MVKO]$_{total}$ / 10^{10} cm^{-3}	[IO]$_0$ / 10^{10} cm^{-3}	σL[MVKO]$_{total}$ / 10^{-4}	1−α	k_3 / s^{-1}	k_{obs} / s^{-1}	A_{BL0} / 10^{-5}
R1	5.9[a]	0[b]	0.0[c]	2.8[d]	N.A.[e]	4.4	0.86	1004	78	4.8
R2	8.4	2.9	1.8	5.6	4.9	8.8	0.82	1370	202	2.9
R3	8.1	5.8	3.8	6.2	9.1	9.7	0.91	1925	474	3.4
R4	8.8	0	0.0	4.5	N.A.	7.1	0.88	1014	93	7.0

[a] Measured with its UV absorption and reported cross sections.[5]

[b] Measured with its UV absorption and reported cross sections.[9]

[c] Estimated with the 352 nm photolysis of NO_2 (σ = 4.53×10^{-17} cm^2 , ϕ = 1).[4,9]

[d] The total amount of MVKO generated via the photolysis of $ICH_2CHCICH_3$ at 352 nm. The value is estimated with the absolute cross sections determined in this work.

[e] Peak value of [IO]. IO was generated from the reaction of $ICH_2CHCICH_3$ and O(^{3}P).

1.4 Summary of the MVKO Experiments

Table S3. Summary of the photodepletion experiments of MVKO. P_{total} = 100 Torr balanced by N_2. P_{O2} = 10 Torr. T = 299 K.

Exp #	[precursor] / 10^{13} cm^{-3}	F_{eff_248} / mJ cm^{-2}	F_{eff_352} / mJ cm^{-2}	N/N_0	$-\Delta$[precursor] / 10^{12} cm^{-3}	[MVKO]$_{total}$ / 10^{11} cm^{-3}	synthesis yield
V1	6.8[a]	3.0[b]	3.4[c]	0.82[d]	4.8[e]	8.9[f]	0.19[g]
V2	6.1	2.6	11.1	0.56	3.7	7.8	0.21
V3	5.8	2.6	10.9	0.56	3.6	7.6	0.21
V4	5.1	2.6	10.9	0.56	3.1	6.8	0.22
V5	5.3	2.6	10.9	0.56	3.2	7.0	0.22
V6	5.4	1.3	11.0	0.54	1.7	3.6	0.21
V7	3.2	1.3	10.9	0.57	1.0	2.3	0.23
V8	5.1	1.3	3.1	0.84	1.6	3.5	0.22
V9	4.8	1.2	18.2	0.37	1.4	3.3	0.23
V10	4.2	1.7	10.9	0.57	1.7	3.8	0.23
V11	2.4	1.6	10.8	0.56	0.9	2.3	0.25
V12	3.5	1.6	7.3	0.67	1.4	3.4	0.25
V13	4.5	1.5	17.8	0.40	1.6	3.9	0.25
V14	4.0	1.6	3.3	0.84	1.5	3.6	0.24

[a] Measured with its UV absorption and reported cross sections.[5]

[b] The effective 248 nm laser fluence.

[c] The effective 352 nm laser fluence.

[d] The survival fraction of MVKO after the 352 nm photodepletion.

[e] Estimated with the 248 nm photolysis of $ICH_2CHCICH_3$ with σ = 1.95×10^{-17} cm^2 and assuming ϕ = 1.[5]

[f] The total amount of MVKO generated via the photolysis of $ICH_2CHCICH_3$ at 248 nm. The value is estimated with the absolute cross sections determined in this work.

[g] Synthesis yield = [MVKO]$_{total}$/($-\Delta$[precursor]).

Table S4. Summary of kinetics of MVKO. The same data as Table S3.

Exp #	delay time / ms	$\sigma L[\text{MVKO}]_{\text{total}}$ / 10^{-3}	$1-\alpha$	data without the 352 nm photolysis			data with the 352 nm photolysis		
				k_3 / s^{-1}	k_{obs} / s^{-1}	A_{BL0} / 10^{-4}	k_3' / s^{-1}	k_{obs}' / s^{-1}	A_{BL0}' / 10^{-4}
V1	0.49[a]	14.0[b]	0.76[b]	2046[b]	429[b]	5.2[b]	2195[c]	428[c]	5.1[c]
V2	1.97	12.4	0.78	1996	343	6.7	2415	306	4.9
V3	2.96	11.9	0.79	1871	346	6.1	1780	291	4.4
V4	3.94	10.8	0.80	1772	327	5.9	1574	263	3.9
V5	1.97	11.1	0.79	1793	339	5.5	2409	303	4.3
V6	1.97	5.6	0.86	1282	208	6.6	1501	199	5.1
V7	1.97	3.6	0.89	1108	161	4.9	1103	150	3.7
V8	1.97	5.5	0.86	1255	205	6.8	1410	203	6.2
V9	1.97	5.3	0.86	1242	196	6.3	1493	186	4.4
V10	1.97	6.1	0.84	1282	213	6.9	1582	196	4.8
V11	1.97	3.6	0.89	1061	170	5.5	1220	156	4.1
V12	1.97	5.4	0.83	1192	213	4.9	1498	202	3.9
V13	2.96	6.1	0.85	1331	225	6.7	1708	179	3.7
V14	2.96	5.7	0.85	1234	215	6.7	1569	201	5.6

[a] The delay time between the 248 nm laser pulse and 352 nm laser pulse.

[b] Fitting range: 0.23–13 ms.

[c] Fitting range: first data points after the 352 nm photolysis to 13 ms.

1.5 MACRO from R20: Photolysis of the Precursor at 352 nm

To quantify the effect of the photolysis of the precursor at 352 nm, we have checked the MACRO signal in the reaction system by changing the first laser wavelength from 248 nm to 352 nm. However, Fig. S4 shows that the 352 nm laser does not produce any observable absorption signal within the probe wavelength range. Therefore, in the analysis of the MACRO photodepletion, we do not include this process.
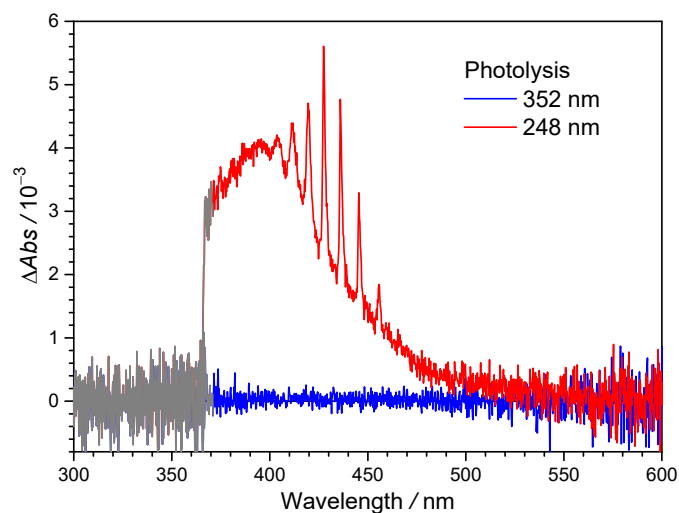

Fig. S4 Difference absorption spectra recorded in the 1,3-diiodo-2-methylprop-1-ene/O_2 photolysis system at 299 K and 502 Torr. [precursor] = 5.2×10^{13} cm^{-3}. The red line shows the data with 248 nm photolysis laser (F_{eff_248} = 4.26 mJ cm^{-2}); the blue line indicates the data with 352 nm photolysis laser (F_{eff_352} = 46.1 mJ cm^{-2}) (only one laser in each experiment). MACRO can be generated via the 248 nm photolysis of the precursor, but no observable MACRO can be generated from the 352 nm photolysis of the precursor. The grey lines indicate the wavelength range where the probe light (λ < 371 nm) was blocked by the longpass filters. Both the spectra have been background-corrected with the SO_2 scavenger method.

1.6 MACRO from R19: Reaction of O(^{3}P) with the Precursor

We have also performed a test experiment for the O(^{3}P)-atom reaction with the MACRO precursor, similar to the case of MVKO. Again, NO$_2$ photolysis was utilized as the source of O(^{3}P) atoms. Here we used SO$_2$ ([SO$_2$] = 1.1×10^{14} cm^{-3}) as a scavenger of MACRO to check if any MACRO was produced. Fig. S5 shows that there is essentially no difference in the absorption signals of the system with and without adding SO$_2$. The absorption can mainly be attributed to that of IO, which is possibly formed from (R19). Based on the reported reaction rate coefficient of MACRO + SO$_2$ (1.5×10^{-10} cm^3 s^{-1}),[1] the lifetime of MACRO would be ca. 0.06 ms. The delay time used in the experiment of Fig. S5 (0.48 ms) is long enough to consume most of MACRO (if it is produced). The indifference in the signals with and without adding SO$_2$ indicates there is no MACRO produced from the O(^{3}P) reaction.
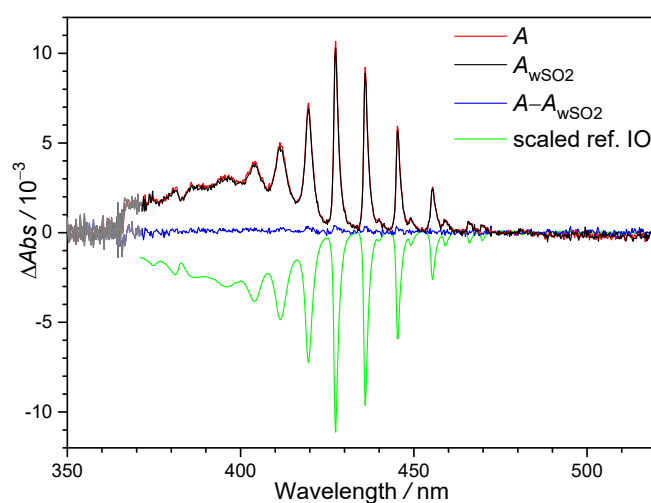
Fig. S5 Difference absorption spectra recorded in the 1,3-diiodo-2-methylprop-1-ene/O$_2$/NO$_2$ system photolyzed at 352 nm (without 248-nm laser) at [precursor] = 3.9×10^{13} cm^{-3}, [NO$_2$] = 1.4×10^{14} cm^{-3}, and F_{eff_352} = 48.6 mJ cm^{-2} at 299 K and 496.7 Torr (balanced by N$_2$), P_{O2} = 10 Torr. The delay time between the 352-nm laser and the probe camera frame is 0.48 ms. SO$_2$ ([SO$_2$] = 1.1×10^{14} cm^{-3}) was used as a scavenger of MACRO. The red line shows the spectrum without SO$_2$, the black line shows the spectrum with SO$_2$, and the blue line indicates their difference. The green line shows the (negatively) scaled reference spectrum of IO.[3] The grey lines indicate the wavelength range where the probe light (λ < 371 nm) was blocked by the longpass filters.
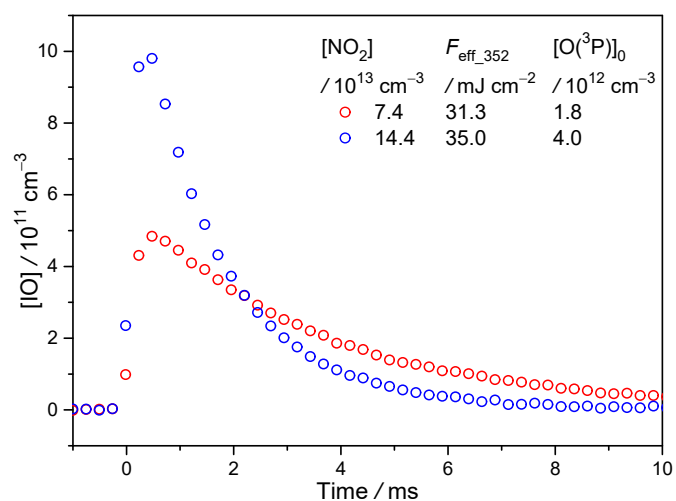
Fig. S6 Time profile of [IO] obtained by fitting the spectra at each camera frame in the 1,3-diiodo-2-methylprop-1-ene/O_2 352-nm photolysis system under various [NO_2] at 299 K and 497.0 Torr (balanced by N_2). P_{O2} = 10 Torr. [precursor] = 3.9×10^{13} cm^{-3}. The time zero is set at the 352 nm photolysis laser pulse. [IO] is derived by comparing with the literature cross section.[3] [O(^{3}P)]$_0$ is estimated with the effective laser fluences and the cross section of NO_2 at 352 nm (4.53×10^{-19} cm^2).[9] With more production of O(^{3}P), more IO is generated, indicating the effect of (R19). The observed yield of IO relative to [O(^{3}P)]$_0$ is (0.26 ± 0.03).

1.7 Summary of the MACRO Experiments

Table S5. Summary of the photodepletion experiments of MACRO. P_{O2} = 10 Torr. T = 299 K.

Exp #	P_{total} / Torr	[precursor] / 10^{13} cm^{-3}	F_{eff_248} / mJ cm^{-2}	F_{eff_352} / mJ cm^{-2}	N/N_0	$-\Delta$[precursor] / 10^{12} cm^{-3}	[MACRO]$_0$ / 10^{11} cm^{-3}	synthesis yield
A1	499[a]	4.5[b]	2.1[c]	24.0[d]	0.51[e]	2.8[f]	1.2[g]	0.044[h]
A2	500	5.2	2.6	23.3	0.47	3.9	1.6	0.042
A3	500	5.1	2.2	23.0	0.56	3.3	1.4	0.042
A4	501	4.5	4.6	19.1	0.54	6.0	2.3	0.039
A5	501	2.3	4.5	19.4	0.60	2.9	1.3	0.046
A6	501	4.4	2.5	19.5	0.58	3.2	1.5	0.046
A7	501	4.4	4.4	19.1	0.58	5.5	2.3	0.043
A8	248	7.9	4.5	16.7	0.62	10.0	2.8	0.028
A9	249	4.1	4.4	16.5	0.62	5.2	1.6	0.032
A10	249	7.7	2.2	16.4	0.66	4.9	1.5	0.031
A11	249	8.0	4.2	16.4	0.62	9.6	2.7	0.028
A12	501	5.2	4.3	45.7	0.34	6.3	2.5	0.039
A13	502	4.8	4.2	30.9	0.42	5.8	2.4	0.042
A14	502	4.4	4.4	47.8	0.31	5.5	2.4	0.043
A15	503	4.5	4.4	15.5	0.65	5.6	2.3	0.041
A16	502	4.5	4.4	26.3	0.47	5.6	2.4	0.042
A17	502	4.5	4.3	37.4	0.38	5.5	2.4	0.043
A18	502	4.4	4.3	46.1	0.32	5.4	2.4	0.043
A19	501	4.4	4.3	17.3	0.59	5.4	2.3	0.043
A20	497	3.8	3.0	48.7	0.32	3.3	1.5	0.046
A21	497	3.7	3.0	15.3	0.60	3.2	1.5	0.045
A22	496	3.7	3.0	31.5	0.44	3.2	1.5	0.047

[a] Balanced by N_2.

[b] Measured with its UV absorption and reported cross sections.[1]

[c] The effective 248 nm laser fluence.

[d] The effective 352 nm laser fluence.

[e] The survival fraction of MACRO after the 352 nm photodepletion.

[f] Estimated with the 248 nm photolysis of ICH$_2$C(CH$_3$)CHI at 248 nm (σ = 2.43×10^{-17} cm^2,[1] assuming ϕ = 1).

[g] The total amount of MACRO generated via the photolysis of ICH$_2$C(CH$_3$)CHI. The value is estimated with the absolute cross section reported in this work.

[h] Synthesis yield = [MACRO]$_0$/($-\Delta$[precursor]).

Table S6. Summary of kinetics of MACRO. The same data as Table S5.

Exp #	delay time / ms	data without the 352 nm photolysis			data with the 352 nm photolysis		
		$\sigma L[\text{MACRO}]_0$ / 10^{-3}	k_{obs} / s^{-1}	A_{BL0} / 10^{-5}	$\sigma L[\text{MACRO}]_0{}'$ / 10^{-3}	k_{obs}' / s^{-1}	A_{BL0}' / 10^{-5}
A1	0.74 [a]	1.59 [b]	589 [b]	3.32 [b]	0.73 [c]	437 [c]	2.93 [c]
A2	0.74	2.12	824	2.56	0.76	468	0.09
A3	1.23	1.77	743	3.68	0.75	520	1.34
A4	0.74	3.02	1146	0.97	1.30	845	0.79
A5	0.74	1.74	751	2.20	0.89	536	2.24
A6	0.49	1.92	800	2.12	1.02	604	0.85
A7	0.49	3.03	1138	1.55	1.56	883	1.17
A8	0.49	3.65	1491	2.34	1.86	1101	1.51
A9	0.49	2.11	952	4.76	1.16	699	−0.82
A10	0.49	1.99	892	2.69	1.18	670	0.18
A11	0.49	3.51	1439	2.35	1.82	1077	2.16
A12	0.49	3.23	1208	0.30	0.85	710	2.81
A13	0.49	3.13	1147	2.49	1.05	666	1.23
A14	0.49	3.10	1172	2.66	0.71	549	−2.93
A15	0.49	2.99	1088	0.88	1.78	896	1.04
A16	0.49	3.07	1136	1.07	1.23	790	1.93
A17	0.49	3.09	1189	3.06	0.89	617	0.28
A18	0.49	3.06	1108	1.59	0.75	555	1.56
A19	0.49	3.04	1101	4.61	1.55	795	0.72
A20	0.49	1.95	836	6.31	0.49	349	−1.25
A21	0.49	1.89	768	1.57	1.03	562	0.90
A22	0.49	1.93	785	3.55	0.74	505	1.75

[a] The delay time between the 248 nm laser pulse and 352 nm laser pulse.

[b] Fitting range: 0.48−10 ms.

[c] Fitting range: first data points after the 352 nm photolysis to 10 ms.
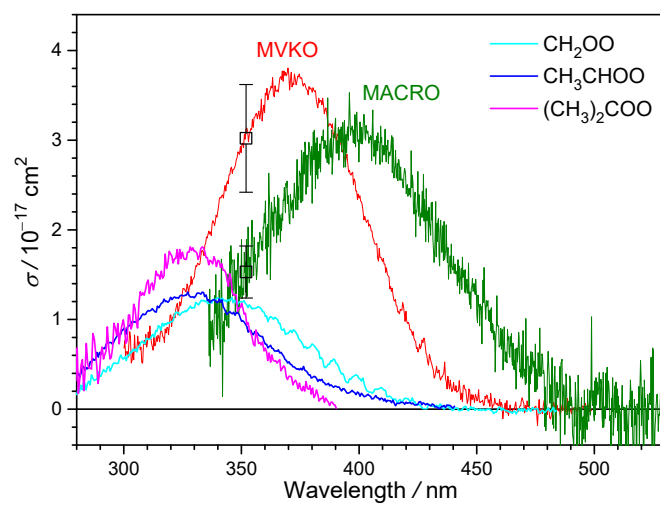
1.8 Comparison of the UV-visible Spectra of 5 CIs

Fig. S7 Comparison of the absorption cross sections of 5 Criegee intermediates: The cross sections of CH_2OO,[10] CH_3CHOO,[11] and $(CH_3)_2COO$[12] are from the literature. The reported spectra[1,2] of MVKO and MACRO are scaled to the absolute values at 352 nm determined in this work (open squares).

2. ERROR DISCUSSION

In the following discussion, SD means the standard deviation of the data set which consists of N data points.

2.1 Error of the Effective Laser Fluence

We used the photodepletion of NO_2 to calibrate the effective laser fluence, F_{eff_352}. (1) The instability of the laser fluence was approximately 3%, estimated by the values measured before and after each experiment. (2) The error of the absolute cross section of NO_2 is approximately 3.4%.[9] (3) The instability of the original $[NO_2]$ was approximately 4%, estimated by the values measured before and after each experiment. (4) The instability of the depleted $[NO_2]$ was approximately 4% (1SD, N = 5).

Assuming the above uncertainties are uncorrelated, the overall error of F_{eff_352} would be $[(3\%)^2 + (3.4\%)^2 + (4\%)^2 + (4\%)^2]^{0.5} = 7\%$.

2.2 Error of σ_{MVKO}

(1) The uncertainty from the spectrum analysis was approximately 5%, estimated by the relative amount of the wavelength independent baseline $A_{BL}(t)$.

(2) The total contribution of R7 and R9 to the MVKO depletion signal is approximately 9%.

$$\frac{A_{R7}(t_{352}) + A_{R9}(t_{352})}{A_{R4}(t_{352})} < 9\%$$

where t_{352} means the time of the 352 nm laser pulse; $A_{R7}(t_{352})$ and $A_{R9}(t_{352})$ represent the MVKO signals generated via the R7 and R9 pathways at t_{352}; $A_{R4}(t_{352})$ indicates the absorption signal of MVKO depleted by the 352 nm photolysis.

We examined the following effects on the determination of the MVKO cross section: (i) the contribution of R7, (ii) the contribution of R9, and (iii) the value of the adduct yield $(1-\alpha)$ of the 352 nm photolysis of the precursor. The results are shown in Fig. S8. In this analysis, the individual contributions of R7 and R9 and $(1-\alpha)$ are scanned (one of them was forced to be amplified or attenuated from its best-estimated value, while other parameters were fixed at their best-estimated values) and the resulted MVKO cross section, which was obtained by linear regression of equation 2b (as the insets of Figures 7 and 10), is plotted as the y-axis value. The R-squared (R^2) value of the linear regression of equation 2b is as good as 0.99 when using the best-estimated parameters. Thus, we believe that the cases with $R^2 < 0.94$ (plotted as open circles) are unreasonable. The cases with $R^2 \geq 0.94$ are plotted as filled circles.
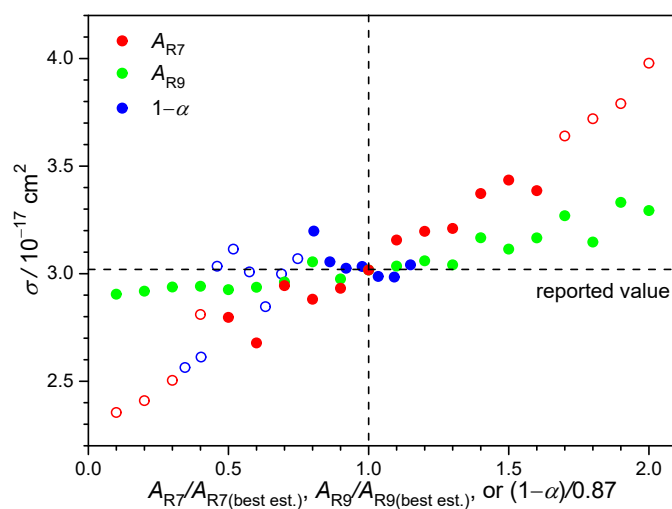
Fig. S8 Effects of R7 and R9 and $(1-\alpha)$ on the determination of the MVKO cross section σ. In this analysis, one of them (A_{R7}, A_{R9}, and $(1-\alpha)$) was forced to be amplified or attenuated from its best-estimated value ($A_{R7(best\ est.)}$, $A_{R9(best\ est.)}$, or 0.87 that is the best estimated value for $1-\alpha$), while other parameters were fixed at their best-estimated values and the resulted MVKO cross section, which was obtained by linear regression of equation 2b (as the insets of Figures 7 and 10), is plotted as the y-axis value. The R-squared (R^2) value of the linear regression of equation 2b is > 0.99 when using the best-estimated parameters. The cases with $R^2 \geq 0.94$ are plotted as filled circles; the cases with $R^2 < 0.94$ are plotted as open circles.

As expected, A_{R7} has the strongest impact on σ. Nonetheless, the contribution of A_{R7} can be determined explicitly from the experimental conditions (described in details in page 12 of the main text). Furthermore, the value of $(1-\alpha)$ has been measured in Exp R1 and R4 ($1-\alpha = 0.86$ and 0.88, respectively, see Table S2). Thus, we believe the uncertainties of these two parameters cannot be worse than 20%, resulting in a deviation of < 7% in σ.

Our confidence on A_{R9} is lower. However, since we have already assumed that the O(^{3}P) yield from the photolyzed MVKO is 100%, higher A_{R9} is unlikely. Lower A_{R9} ($A_{R9}/A_{R9(best\ est.)} = 0$ to 1) is possible and its impact on σ is within 3%, as shown in Fig. S8. Overall, we accessed the uncertainty in σ due to the uncertainties in A_{R7}, A_{R9} and $(1-\alpha)$ should be less than 7%.

(3) There is a minor contribution of the time independent baseline A_{BL0} to the observed peak absorbance of MVKO $A_{obs}(t)$. Since we are not very sure about the sources of A_{BL0}, we may consider its effect in the cross-section determination as an error bar. If we did not consider A_{BL0} (force A_{BL0} be zero) in the analysis, the resulting cross section would be 7% smaller.

(4) The reproducibility of our results was estimated to be approximately 3% (1SD, N = 14) obtained by applying eqn (2b) to each data point (Table S3, Fig. 7).

Finally, if we assume the above uncertainties (5% due to the spectrum analysis ($A_{\mathrm{BL}}(t)$), 7% due to the modeling, 7% due to A_{BL0}, and 3% due to the data reproducibility) are uncorrelated and also considering the 7% error from $F_{\mathrm{eff\_352}}$, the total error would be $[(5\%)^2 + (7\%)^2 + (7\%)^2 + (3\%)^2 + (7\%)^2]^{0.5} = 13\%$. However, this error bar may be too optimistic because the following factors may cause a larger uncertainty.

(i) The kinetic model may be a bit too simple;

(ii) Some of the above errors may be correlated, especially the first three terms (the last two terms, data reproducibility and $F_{\mathrm{eff\_352}}$, are likely uncorrelated to others);

(iii) Most of the above error bars are only based on 1SD of the data.

If we assume the first three errors are correlated, the overall error may become $[(5\%+ 7\%+ 7\%)^2 + (3\%)^2 + (7\%)^2]^{0.5} = 20\%$. It is hard to give any more quantitative estimation. Thus, we report an error bar of $\pm20\%$ for the cross section of MVKO at 352 nm.

2.3 Error of σ_{MACRO}

(1) The uncertainty from the spectrum analysis is estimated to be 15% by the relative amount of the wavelength independent baseline $A_{\text{BL}}(t)$.

(2) From Fig. S4, we found that the absorption signal of MACRO from the 352-nm photolysis (R20: $\text{ICH}_2\text{C}(\text{CH}_3)\text{CHI} + h\nu\,(352\text{ nm}) \rightarrow \text{CH}_2=\text{C}(\text{CH}_3)\text{CHI} + \text{I}$) is smaller than 10^{-5}, which is at least 50 times smaller than the signal of MACRO from the 248-nm photolysis (see Fig. 9 and Table S6). Thus, we think the uncertainty from (R20) is negligible.

(3) Considering the generation of MACRO from the reaction of $\text{O}(^3\text{P})$ with the precursor (R19: $\text{O}(^3\text{P}) + \text{ICH}_2\text{C}(\text{CH}_3)\text{CHI} \rightarrow \text{IO} + \text{products}$), from Fig. S5, the maximum absorption signal of MACRO from this reaction is estimated to be 5×10^{-5}. The amount of $\text{O}(^3\text{P})$ generated from the 352 nm photolysis of MACRO ($[\text{O}(^3\text{P})] < 2\times10^{11}$ cm^{-3}) is estimated to be at least fifteen times smaller than that of Fig. S5 ($[\text{O}(^3\text{P})] = 3\times10^{12}$ cm^{-3}). Thus, the maximum signal of MACRO generated from (R19) is much smaller than that generated from the 248-nm photolysis (see Fig. 9 and Table S6), and thus the uncertainty from this reaction can be neglected.

(4) The contribution of the time independent baseline A_{BL0} to the observed peak absorbance of MACRO $A_{\text{obs}}(t)$ is small, with its effect in the cross-section values being less than 1% (thus negligible). We believe that this is because the signal of MACRO has been extracted with the SO_2 scavenger method.

(5) The reproducibility of our results is approximately 10% (1SD, N = 22) by applying eqn (2b) to each data point (Fig. 10 and Table S5) to obtain the absolute cross section. Note that the signals of MACRO are much weaker than those of MVKO, leading to worse reproducibility of the MACRO cross-section results.

Assuming the above uncertainties are uncorrelated and considering the 7% error from $F_{\text{eff\_352}}$, the total error will be $[(15\%)^2 + (10\%)^2 + (7\%)^2]^{0.5} = 19\%$.

2.4 Error for the Synthesis Yield of MVKO

Assume $\phi = 1$ for the 248-nm photolysis of the precursor $\text{ICH}_2\text{CHCICH}_3$.

(1a) The concentration of $\text{ICH}_2\text{CHCICH}_3$ was determined by measuring its UV absorption in a cell and considering the dilution between the cell and the reactor. The error of the spectrum analysis is approximately 5%, and that of dilution is approximately 2%. The absolute cross section of $\text{ICH}_2\text{CHCICH}_3$ is from the literature, and the reported uncertainty is 2%.[5] (1b) The uncertainty of the effective 248 nm laser fluence is estimated to be 40% because the calibration cannot be applied in this experimental setup. The uncertainty of the photolyzed precursor is therefore $[(5\%)^2 + (2\%)^2 + (2\%)^2 + (40\%)^2]^{0.5} = 40\%$.

(2) The amount of generated [MVKO] is estimated with its absorption spectrum, effective light path, absolute cross section, and the kinetic analysis. The error from the absolute cross section (20%) is dominant, and we neglect other errors.

Assuming the above uncertainties are uncorrelated, the error of the synthesis yield of MVKO is $[(40\%)^2 + (20\%)^2]^{0.5} = 45\%$.

2.5 Error for the Synthesis Yield of MACRO

(1) The analysis of the uncertainty of the photolyzed $ICH_2C(CH_3)CHI$ (MACRO precursor) is similar to the above discussion for $ICH_2CHCICH_3$. The reported error from the literature absolute cross section of $ICH_2C(CH_3)CHI$ is 7%.[1] The total uncertainty of the photolyzed $ICH_2C(CH_3)CHI$ is $[(5\%)^2 + (2\%)^2 + (7\%)^2 + (40\%)^2]^{0.5} = 41\%$.

(2) For the estimation of the generated [MACRO], the error of the absolute cross section (19%) is dominant.

Assuming the above uncertainties are uncorrelated, the error of the synthesis yield of MACRO is $[(41\%)^2 + (19\%)^2]^{0.5} = 45\%$.

3. SUMMARY OF THEORETICAL RESULTS AND DETAILS

3.1 Thermal Populations of *syn*-MVKO and *anti*-MACRO Conformers

To obtain the thermal population of *syn*-MVKO and *anti*-MACRO, we followed our previous theoretical study on MVKO.[6, 7] The geometries were optimized at the B2PLYP[13] level with Grimme's empirical D3 dispersion correction with Becke-Johnson damping (D3BJ),[14] using Dunning's cc-pVTZ basis set.[15] We performed energy correction on the B2PLYP geometries using the explicitly correlated coupled cluster singles and doubles with perturbative triples, CCSD(T)-F12b method[16] with the cc-pVTZ-F12 basis sets. Using these electronic energies and the harmonic frequencies obtained from B2PLYP-D3BJJ/cc-pVTZ, we obtain the 0 K enthalpy difference for the *syn*-MVKO and *anti*-MACRO conformers.

(1) *Syn-cis*-MVKO is 1.75 kcal mol^{-1} higher than *syn-trans*-MVKO;

(2) *Anti-cis*-MACRO is 3.17 kcal mol^{-1} higher than *anti-trans*-MACRO.

These values are very close to the literature values, 1.76[17] and 3.18[18] kcal mol^{-1} by Lester and coworkers, who used CCSD(T)-F12 energies extrapolated from the cc-pVTZ-F12 and cc-pVQZ-F12 basis sets at geometries optimized by B2PLYP-D3/cc-pVTZ.

Using our level of theory mentioned above, we obtained the following for the 298 K free energy difference ΔG^o(298 K) at the standard state.

(1) *Syn-cis*-MVKO is 1.41 kcal mol^{-1} higher than *syn-trans*-MVKO;

(2) *Anti-cis*-MACRO is 2.82 kcal mol^{-1} higher than *anti-trans*-MACRO.

Using these ΔG^o(298 K), the population of the conformers are estimated to be 0.085 (*syn-cis*-MVKO): 0.915 (*syn-trans*-MVKO) and 0.008 (a*nti-cis*-MACRO): 0.992 (*anti-trans*-MACRO).
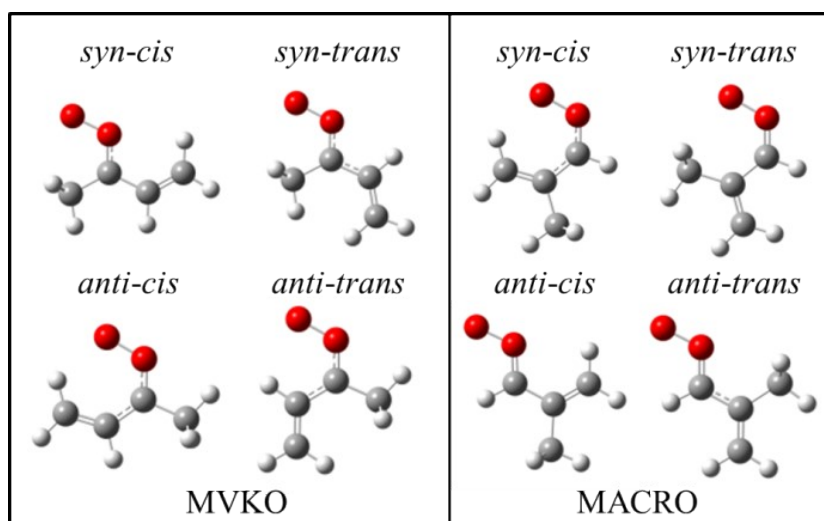

Fig. S9 Conformers of MVKO and MACRO. The geometries are calculated by B3LYP/6-311+G(2d,2p).

3.2 Conformer Dependence in the Electronic Spectra of MVKO and MACRO

Table S7. Conformer-dependent excitation energies, spectral widths (full width at half maximum, FWHM) and oscillator strengths of MVKO and MACRO electronic transitions calculated by using the EOM-CCSD/aug-cc-pVTZ method. The ground-state geometries were optimized using the QCISD(T)/aug-cc-pVTZ method.

	MVKO				MACRO			
	syn-trans	*syn-cis*	*anti-trans*	*anti-cis*	*anti-trans*	*anti-cis*	*syn-trans*	*syn-cis*
excitation energy / eV	3.786	3.527	3.392	3.650	3.505	3.304	3.542	3.741
FWHM / eV	0.366	0.297	0.274	0.292	0.386	0.381	0.360	0.401
oscillator strength	0.335	0.224	0.211	0.141	0.311	0.248	0.245	0.164
thermal population	0.915[a]	0.085[a]	–[b]	–[b]	0.992[a]	0.008[a]	–[b]	–[b]

[a] Their thermal populations are estimated with ΔG^o(298 K) mentioned above (section 3.1).

[b] These conformers are unstable, forming a COOCC five-membered ring within less than 10^{-3} s.[19]

Table S8. Literature values for the electronic excitation energies and oscillator strengths of CH_2OO, MVKO conformers, and MACRO conformers calculated at CASPT2 (12,10)/aug-cc-pVDZ.[17, 18, 20, 21]

	CH_2OO	MVKO				MACRO			
		syn-trans	*syn-cis*	*anti-trans*	*anti-cis*	*anti-trans*	*anti-cis*	*syn-trans*	*syn-cis*
excitation energy / eV									
Vansco et al.[17]	–	3.54	3.25	3.16	3.31	–	–	–	–
Vansco et al.[18]	–	–	–	–	–	3.31	3.26	3.29	3.62
McCoy et al.[20]	–	3.32	3.05	2.79	3.13	3.05	2.97	3.32	3.08
McCoy et al.[21]	3.74	–	–	–	–	–	–	–	–
oscillator strength									
Vansco et al.[17]	–	0.147	0.111	0.211	0.070	–	–	–	–
Vansco et al.[18]	–	–	–	–	–	0.116	0.093	0.094	0.057
McCoy et al.[20]	–	0.139	0.116	0.092	0.073	0.127	0.107	0.101	0.068
McCoy et al.[21]	0.082	–	–	–	–	–	–	–	–

3.3 Formation Processes of MVKO and MACRO

To understand the differences in the formation processes of the different CIs, we followed our previous theoretical study, which compared CH_2OO versus MVKO.[6] We have calculated the stationary points for the precursor radicals (CH_2I, CH_3CHI $(CH_3)_2CI$, $CH_3(C_2H_3)CI$, and $CH_2=C(CH_3)CHI$), the O_2 adducts (CH_2IOO CH_3CHIOO $(CH_3)_2CIOO$, $CH_3(C_2H_3)CIOO$, and $CH_2=C(CH_3)CHIOO$), as well as the respective Criegee intermediate products (CH_2OO, CH_3CHOO, $(CH_3)_2COO$, $CH_3(C_2H_3)COO$, and $CH_2=C(CH_3)CHOO$) using the B2PLYP[13] method using Dunning's cc-pVTZ basis set[15] for C, H and O while the pseudopotential-based cc-pVTZ-PP[22] was used for the I atom. We included Grimme's empirical D3 dispersion correction with Becke-Johnson damping (D3BJ).[14] The oxygen molecule was optimized at the triplet ground electronic state, while the precursor radicals, adducts, and iodine atom were optimized at the doublet ground electronic states, and the Criegee intermediates were optimized at the singlet ground electronic states. To obtain accurate reaction energies, we performed energy correction on the B2PLYP-D3BJ geometries using the explicitly correlated coupled cluster singles and doubles with perturbative triples, CCSD(T)-F12b method[16] with the cc-pVTZ-F12 basis sets for C, H, O, and the cc-pVTZ-PP-F12 for I.[23, 24] In our previous study, we found that the heat of reaction for $CH_2I + O_2 \rightarrow CH_2IOO$, and $CH_2OO + I \rightarrow CH_2IOO$ reactions obtained by the triple zeta basis set can be off by at most 1 kcal mol^{-1} compared to the results at the complete basis set limit, indicating the error of using the cc-pVTZ-F12 energies instead of the complete basis set limit value may give an order of magnitude error in the calculated equilibrium constants. However, we believe that the trend of different substituents will be properly calculated using the cc-pVTZ-F12 basis set. The energy of the iodine atom was corrected for the spin-orbit coupling using the recommended value of 7.24 kcal mol^{-1} given in the Computational Chemistry Comparison and Benchmark Data Base.[25]

Table S9. Calculated relative energies $\Delta H°$, standard free energies $\Delta G°$, and equilibrium constants K_{eq} for the adduct channels of the CH_2OO, *syn*-CH_3CHOO, $(CH_3)_2COO$, MVKO, and MACRO synthesis systems.

Reactions	$\Delta H°$(0 K) /kcal mol⁻¹	$\Delta G°$(298 K) /kcal mol⁻¹	K_{eq}(298 K) /cm³	[adduct] /[R₁R₂CI]	[R₁R₂COO] /[R₁R₂CI]
$CH_2I + O_2 \rightarrow CH_2IOO$	−26.4[a]	−16.4[a]	$2.84\times10^{-8,b}$	$8.52\times10^{9,c}$	
$CH_2OO + I \rightarrow CH_2IOO$	−27.3	−20.5	2.58×10^{-5}		55.0^d
$CH_3CHI + O_2 \rightarrow CH_3CHIOO$	−29.5	−19.1	2.55×10^{-6}	7.65×10^{11}	
syn-$CH_3CHOO + I \rightarrow CH_3CHIOO$	−22.1	−14.9	2.32×10^{-9}		5.50×10^{7}
$(CH_3)_2CI + O_2 \rightarrow (CH_3)_2CIOO$	−30.0	−18.8	1.73×10^{-6}	5.18×10^{11}	
$(CH_3)_2COO + I \rightarrow (CH_3)_2CIOO$	−18.6	−10.7	2.27×10^{-12}		3.80×10^{10}
$CH_3(C_2H_3)CI + O_2 \rightarrow CH_3(C_2H_3)CIOO$	−15.5	−4.8	1.15×10^{-16}	34.6	
$CH_3(C_2H_3)COO + I \rightarrow CH_3(C_2H_3)CIOO$	−14.0	−6.2	1.24×10^{-15}		4.65×10^{3}
$CH_2=C(CH_3)CHI + O_2 \rightarrow CH_2=C(CH_3)CHIOO$	−16.4	−6.6	2.59×10^{-15}	7.78×10^{2}	
$CH_2=C(CH_3)CHOO + I \rightarrow CH_2=C(CH_3)CHIOO$	−19.3	−12.4	4.39×10^{-11}		2.95

[a] At CCSD(T)-F12b/cc-pVTZ-F12//B2PLYP/cc-pVTZ level including an empirical spin–orbit correction for I atom.

[b] For example, K_{eq} = [CH₂IOO]/([CH₂I][O₂]).

[c] For example, [adduct]/[R₁R₂CI] means [CH₂IOO]/[CH₂I]. The values are at [O₂] = 3×10^{17} cm⁻³ (typical value used in the experiments).

[d] At [O₂] = 3×10^{17} cm⁻³ and [I] = 6×10^{12} cm⁻³ (two times the median value of the depleted precursor). For example, [R₁R₂COO]/[R₁R₂CI] means [CH₂OO]/[CH₂I].

3.4 Details Concerning the Complete Active Space

Since we are interested in the energy range of the first excited A' and A" states (2A' and 1A" states), a 5-state averaging of three A' and two A" states were used in the CASSCF. One extra higher-energy state for each symmetry was included to stabilize the target states. Following Dawes et al.,[26] we used a dynamical weighting of 3 eV. The selection of active orbitals in the CASSCF and MRCI becomes critical, and ideally, one would prefer full valance active space. However, even for CH_2OO, the full valance is very large, 18 electrons in 14 orbitals (18e 14o). As shown in Table S10, we have evaluated different active spaces, using the same active space for CASSCF and MRCI. We found that for CH_2OO, an active space of 10 electrons 10 orbitals (10e 10o) would give results within approximately 0.03 eV of the full valance results in peak position. This (10e 10o) active space corresponds to closing all 1s, all three 2s, and one extra in-plane 2p orbitals, or in molecular orbital (MO) picture it means that in addition to the core orbitals, we close the valance MOs corresponding to σ_{OO}, σ_{CO}, σ_{CH1}, and σ_{CH2}. It is important to note that if we use Hartree-Fock orbitals instead of CASSCF orbitals and perform the (10e10o) MRCI calculation (last row of Table S10), we get a peak position that is approximately 0.1 eV lower than the full valance result, and the oscillator strength is overestimated. This latter point is because the single reference methods tend to overestimate the zwitterionic (C^+–O–O^-) contribution leading to larger charge separation between the terminal oxygen and the carbonyl carbon. The strong transition from the 1A' ground state to the 2A' excited state can be assigned mainly to the electron transition from the terminal oxygen out-of-plane 2p orbital to the carbonyl anti-bonding (out-of-plane) π^* orbital, so it is expected that overestimating the zwitterionic contribution would overestimate the oscillator strength. This is consistent with the fact that the single reference methods, such as EOM-CCSD and TD-CAMB3LYP, also overestimate the oscillator strength.

Before ending this section, we would like to note that Hartree-Fock-orbital-based MRCI+Q seems to give a spectral width more consistent to the experimental result; but this is due to the cancellation of errors. As we can see, the full valance results give a slightly narrow width. Furthermore, our previous two-dimensional wave packet study, including the COO bending mode to the OO bond distance, gave wider UV spectra compared to those obtained by only considering the OO bond distance.[27] Thus, for CH_2OO, we believe the difference in the spectral width compared to the experimental result is due to the reduced dimension of the calculation, not a limitation of the quantum chemistry calculation.

Table S10. Comparison of the theoretical excitation energies, spectral widths (full width at half maximum, FWHM), and oscillator strengths obtained with the MRCI+Q method using different active spaces for CH_2OO.

	excitation energy / eV	FHWM / eV	oscillator strength
Experimental	3.68	0.89	0.10
(14e 18o) (full valence)	3.66	0.67	0.11
(10e 10o)	3.64	0.67	0.12
(8e 8o)	3.66	0.67	0.12
(6e 6o)	3.69	0.66	0.11
HF (10e 10o)*	3.58	0.82	0.15

*HF orbitals were used in the MRCI+Q calculations; all others used CASSCF orbitals.

For CH_3CHOO, the full valance active space would be (24e 20o). If one wants to perform a calculation equivalent to the (10e 10o) active space of CH_2OO, we need to close four 2s orbitals and one extra in-plane 2p orbital resulting in (14e 15o) active space. In the MO picture, this active space means that we close the core orbitals and the valance MOs corresponding to σ_{OO}, σ_{CO}, σ_{CH1}, σ_{CC}, and $\sigma_{CHmethyl}$, where the last CH bonds are for the terminal methyl group. Unfortunately, our computational resources did not allow such calculations, even for CH_3CHOO. Considering the accuracy and our computational resources, we have decided to use (10e 10o) active space for all other CIs, CH_3CHOO, $(CH_3)_2COO$, MVKO, and MACRO. We note that a recent study using perturbation correction to CASSCF (CASPT2) has used an active space similar to our present (10e 10o) space: (12e 10o) was used for CH_2OO, MVKO, and MACRO.[17, 18, 20, 21, 28-30]

3.5 Discussion on the Effect of Geometry

We have used two methods (B3LYP and QCISD(T)) to obtain the equilibrium ground electronic state geometry in the present study. From Fig. S10, where we compare the EOM-CCSD results of the electronic transitions, we can see that the two geometries result in minor differences for the oscillator strengths. We see a systematic blue shift by approximately 0.1 eV for the peak position obtained using the B3LYP geometries compared to the QCISD(T) geometries. Also the FWHM values obtained using B3LYP geometries are larger by approximately 0.03eV. Since QCISD(T) is a more accurate method, we used QCISD(T) results in the main text.
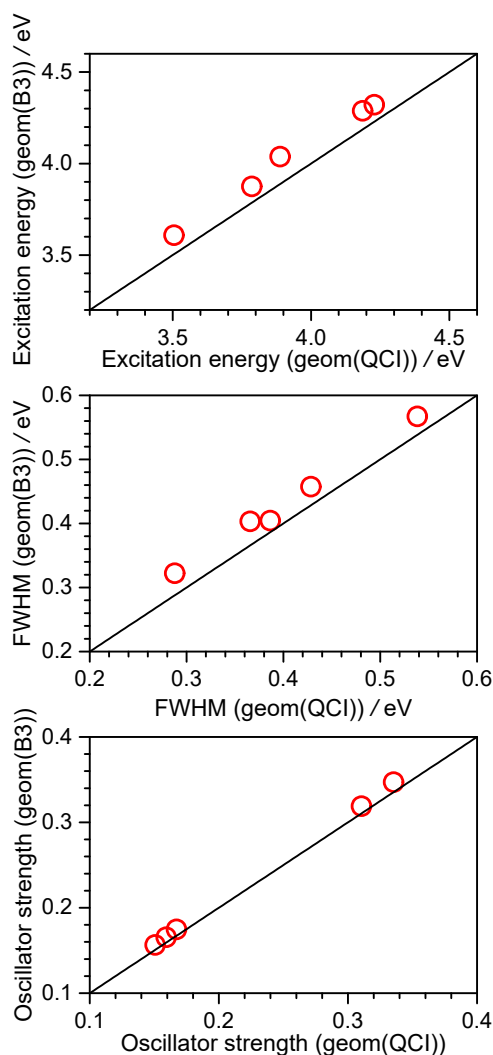
Fig. S10 Comparison of the theoretical oscillator strengths, transition energies, and spectral widths (full width at half maximum, FWHM) calculated using EOM-CCSD with different equilibrium geometries for 5 CIs. X-axis is from the geometries by QCISD(T), while Y-axis from those by B3LYP. Diagonal lines are plotted to guide the eye.

3.6 Discussion on the Calculated UV Spectra Width

To understand why the MRCI+Q calculation results in a wider width compared to the other two single reference methods, we have to look back at eqn (3) in the main text. We can see that the width is directly related to the gradient of the electronically excited state at the ground electronic state equilibrium geometry. In Fig. S11, we present the 1-dimensional potential energy curve along the OO bond calculated by using three methods for CH_2OO. Other than the fact that the potential energy curves calculated by TD-CAMB3LYP and EOM-CCSD are at slightly higher energies than MRCI+Q, we can notice that the positions of the excited state minima are different. For these single-reference-based methods, the minima on the excited state are closer to the ground electronic state minima. Therefore, in the Franck-Condon region, the excited state is not as repulsive as the MRCI+Q potential energy curve, for which the excited state minimum is at a slightly longer bond length. This

difference in the characteristics of the excited electronic states causes a smaller gradient for TD-CAMB3LYP and EOM-CCSD and results in a narrower width in the calculated UV spectra.
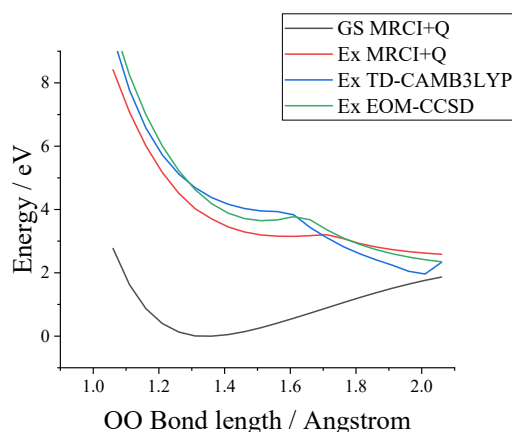

Fig. S11 Potential energy curves along the OO bond length for CH_2OO calculated by using MRCI+Q for the ground state (black) and excited state (red), as well as those calculated by TD-CAMB3LYP (blue) and EOM-CCSD (green) for the excited state. Since the ground state potential energy curves calculated using CAMB3LYP and CCSD are similar to the MRCI+Q one, we only present the MRCI+Q curve.

We discuss numerical details used to obtain the excited state gradient V'. In the present calculation, we used $\Delta R = 0.1$Å and utilized the central numerical differentiation using ($R_{eq} \pm 0.1$Å) to obtain V', which is the average of the forward (using R_{eq} and $R_{eq}+0.1$Å) and backward (using R_{eq} and $R_{eq}-0.1$Å) numerical differentiations. As shown in Table S11, the values of forward and backward numerical derivatives are very different for $\Delta R = 0.1$Å. However, as can be seen from the convergence, central differentiation at $\Delta R = 0.1$Å can give a value consistent with those at $\Delta R = 0.01$Å. The FWHM calculated using the central numerical differentiation only varies by 0.02 eV in going from $\Delta R = 0.1$Å to 0.01Å. The values for MVKO, given in Table S12, also show that our numerical derivatives are consistent, and we obtain the qualitative trend that MVKO has a narrower width than CH_2OO. In addition, we can also confirm that the calculated harmonic frequencies for the OO stretching mode are consistent with the experimental IR peak positions of 908 and 942 cm^{-1} for CH_2OO[31] and MVKO,[32] respectively. Here, the experimental peak position includes mode coupling of the OO stretching coordinate with other vibrational modes such as COO bending, so it is slightly lower. In our previous study,[27] we obtained unphysical frequencies when we used a small ΔR for the MRCI+Q calculations using QCISD(T) geometries, so we used $\Delta R = 0.1$Å in this study. This is due to the difference in the optimized OO distance between MRCI+Q and QCISD(T). Ideally, we would like to use MRCI+Q optimized geometries, but that is beyond our computational resources for the larger MVKO and MACRO. We also list the convergence test using EOM-CCSD and MRCI+Q for CH_2OO in Table S11, and can confirm that the large difference in width comes from the difference in the V' calculated by MRCI+Q versus the single reference methods, not due to errors in our numerical differentiation.

Table S11. Comparison of the numerical derivative values V′ obtained by different ΔR for CH_2OO calculated using TD-CAMB3LYP/6-311+G(2d,2p). Results by EOM-CCSD and MRCI+Q are given in parenthesis and square brackets.

ΔR / Å	Backward V′ / Hartree bohr^{-1}	Forward V′ / Hartree bohr^{-1}	Central V′ / Hartree bohr^{-1}	Harmonic Frequency / cm^{-1}	FWHM by central V′ / eV
0.1	0.101 (0.144) [0.161]	0.041 (0.047) [0.079]	0.0712 (0.095) [0.120]	980 (968) [983]	0.40 (0.54) [0.67]
0.05	0.082 (0.116) [0.133]	0.054 (0.068) [0.095]	0.0680 (0.092) [0.114]	966 (953) [942]	0.38 (0.52) [0.65]
0.02	0.073 (0.101) [0.123]	0.061 (0.081) [0.107]	0.0672 (0.091) [0.115]	962 (948) [971]	0.38 (0.52) [0.65]
0.01	0.070 (0.096) [0.119]	0.064 (0.086) [0.111]	0.0670 (0.091) [0.115]	962 (939) [971]	0.38 (0.52) [0.65]

Table S12. Comparison of the numerical derivative values V′ obtained by different ΔR for MVKO calculated using TD-CAMB3LYP/6-311+G(2d,2p).

ΔR / Å	Backward V′ / Hartree bohr^{-1}	Forward V′ / Hartree bohr^{-1}	Central V′ / Hartree bohr^{-1}	Harmonic Frequency / cm^{-1}	FWHM by central V′ / eV
0.10	0.073	0.015	0.044	971	0.25
0.05	0.055	0.027	0.041	958	0.23
0.02	0.046	0.034	0.040	954	0.23
0.01	0.043	0.037	0/040	962	0.23

4. REFERENCES

1. Y.-H. Lin, C. Yin, K. Takahashi and J. J.-M. Lin, *Comm. Chem.*, 2021, **4**, 12.

2. R. L. Caravan, M. F. Vansco, K. Au, M. A. H. Khan, Y.-L. Li, F. A. F. Winiberg, K. Zuraski, Y.-H. Lin, W. Chao, N. Trongsiriwat, P. J. Walsh, D. L. Osborn, C. J. Percival, J. J.-M. Lin, D. E. Shallcross, L. Sheps, S. J. Klippenstein, C. A. Taatjes and M. I. Lester, *Proc. Nat. Acad. Sci. U. S. A.*, 2020, **117**, 9733-9740.

3. P. Spietz, J. C. Gómez Martín and J. P. Burrows, *J. Photochem. Photobiol. A*, 2005, **176**, 50-67.

4. S. P. Sander, J. Abbatt, J. R. Barker, J. B. Burkholder, R. R. Friedl, D. M. Golden, R. E. Huie, C. E. Kolb, M. J. Kurylo, G. K. Moortgat, V. L. Orkin and P. H. Wine, Chemical Kinetics and Photochemical Data for Use in Atmospheric Studies, *Evaluation Number 17*, JPL Publication 10-6, Jet Propulsion Laboratory, Pasadena, 2011, http://jpldataeval.jpl.nasa.gov/.

5. M.-T. Kuo, J.-N. Yang, J. J.-M. Lin and K. Takahashi, *J. Phys. Chem. A*, 2021, **125**, 6580-6590.

6. Y.-H. Lin, Y.-L. Li, W. Chao, K. Takahashi and J. J.-M. Lin, *Phys. Chem. Chem. Phys.*, 2020, **22**, 13603-13612.

7. Y.-H. Lin, C.-H. Yang, K. Takahashi and J. J.-M. Lin, *J. Phys. Chem. A*, 2020, **124**, 9375-9381.

8. M. A. Teruel, T. J. Dillon, A. Horowitz and J. N. Crowley, *Phys. Chem. Chem. Phys.*, 2004, **6**, 2172-2178.

9. K. Bogumil, J. Orphal, T. Homann, S. Voigt, P. Spietz, O. C. Fleischmann, A. Vogel, M. Hartmann, H. Kromminga, H. Bovensmann, J. Frerick and J. P. Burrows, *J. Photochem. Photobiol. A*, 2003, **157**, 167-184.

10. W.-L. Ting, Y.-H. Chen, W. Chao, M. C. Smith and J. J.-M. Lin, *Phys. Chem. Chem. Phys.*, 2014, **16**, 10438-10443.

11. M. C. Smith, W.-L. Ting, C.-H. Chang, K. Takahashi, K. A. Boering and J. J.-M. Lin, *J. Chem. Phys.*, 2014, **141**, 074302.

12. Y.-P. Chang, C.-H. Chang, K. Takahashi and J. J.-M. Lin, *Chem. Phys. Lett.*, 2016, **653**, 155-160.

13. S. Grimme, *J. Chem. Phys.*, 2006, **124**, 034108.

14. S. Grimme, J. Antony, S. Ehrlich and H. Krieg, *J. Chem. Phys.*, 2010, **132**, 154104.

15. T. H. Dunning, *J. Chem. Phys.*, 1989, **90**, 1007-1023.

16. G. Knizia, T. B. Adler and H. J. Werner, *J. Chem. Phys.*, 2009, **130**, 054104.

17. M. F. Vansco, B. Marchetti and M. I. Lester, *J. Chem. Phys.*, 2018, **149**, 244309.

18. M. F. Vansco, B. Marchetti, N. Trongsiriwat, T. Bhagde, G. Wang, P. J. Walsh, S. J. Klippenstein and M. I. Lester, *J. Am. Chem. Soc.*, 2019, **141**, 15058-15069.

19. M. F. Vansco, R. L. Caravan, K. Zuraski, F. A. F. Winiberg, K. Au, N. Trongsiriwat, P. J. Walsh, D. L. Osborn, C. J. Percival, M. A. H. Khan, D. E. Shallcross, C. A. Taatjes and M. I. Lester, *J. Phys. Chem. A*, 2020, **124**, 3542-3554.

20. J. C. McCoy, S. J. Léger, C. F. Frey, M. F. Vansco, B. Marchetti and T. N. V. Karsili, *J. Phys. Chem. A*, 2022, DOI: 10.1021/acs.jpca.1c08381.

21. J. C. McCoy, B. Marchetti, M. Thodika and T. N. V. Karsili, *J. Phys. Chem. A*, 2021, **125**, 4089-4097.

22. K. A. Peterson, B. C. Shepler, D. Figgen and H. Stoll, *J. Phys. Chem. A*, 2006, **110**, 13877-13883.

23. K. A. Peterson, T. B. Adler and H. J. Werner, *J. Chem. Phys.*, 2008, **128**, 084102.

24.   J. G. Hill and K. A. Peterson, *J. Chem. Phys.*, 2014, **141**, 094106.

25.   Https://cccbdb.nist.gov.

26.   R. Dawes, B. Jiang and H. Guo, *J. Am. Chem. Soc.*, 2014, **137**, 50-53.

27.   C. Yin and K. Takahashi, *Phys. Chem. Chem. Phys.*, 2018, **20**, 16247-16255.

28.   V. J. Esposito, O. Werba, S. A. Bush, B. Marchetti and T. N. V. Karsili, *Photochem. Photobiol.*, 2021, https://doi.org/10.1111/php.13560

29.   V. J. Esposito, T. Liu, G. Wang, A. Caracciolo, M. F. Vansco, B. Marchetti, T. N. V. Karsili and M. I. Lester, *J. Phys. Chem. A*, 2021, **125**, 6571-6579.

30.   G. Wang, T. Liu, A. Caracciolo, M. F. Vansco, N. Trongsiriwat, P. J. Walsh, B. Marchetti, T. N. V. Karsili and M. I. Lester, *J. Chem. Phys.*, 2021, **155**, 174305.

31.   Y.-T. Su, Y.-H. Huang, H. A. Witek and Y.-P. Lee, *Science*, 2013, **340**, 174-176.

32.   C.-A. Chung and Y.-P. Lee, *Comm. Chem.*, 2021, **4**, 8.